Hydrodynamic slip length as a surface property

Bladimir Ramos-Alvarado,* Satish Kumar, and G. P. Peterson
The George W. Woodruff School of Mechanical Engineering, Georgia Institute of Technology, Atlanta, Georgia 30332, USA
(Received 9 December 2015; published 1 February 2016)

Equilibrium and nonequilibrium molecular dynamics simulations were conducted in order to evaluate the hypothesis that the hydrodynamic slip length is a surface property. The system under investigation was water confined between two graphite layers to form nanochannels of different sizes (3–8 nm). The water-carbon interaction potential was calibrated by matching wettability experiments of graphitic-carbon surfaces free of airborne hydrocarbon contamination. Three equilibrium theories were used to calculate the hydrodynamic slip length. It was found that one of the recently reported equilibrium theories for the calculation of the slip length featured confinement effects, while the others resulted in calculations significantly hindered by the large margin of error observed between independent simulations. The hydrodynamic slip length was found to be channel-size independent using equilibrium calculations, i.e., suggesting a consistency with the definition of a surface property, for 5-nm channels and larger. The analysis of the individual trajectories of liquid particles revealed that the reason for observing confinement effects in 3-nm nanochannels is the high mobility of the bulk particles. Nonequilibrium calculations were not consistently affected by size but by noisiness in the smallest systems.

DOI: 10.1103/PhysRevE.93.023101

I. INTRODUCTION

The Navier-Stokes (NS) equations and the no-slip boundary condition represent a cornerstone of the classical fluid dynamics. By applying a no-slip boundary condition, experiments and numerical or analytical models have been reconciled for a number of applications. The robustness of the NS equations can be verified by identifying the lower-scale limit for the validity of the notion of viscosity. Bocquet and Charlaix [1] used a simple scale analysis to demonstrate that the NS equations can be valid at confinement levels down to $\sim$1 nm for water, and Thomas and McGaughey [2] confirmed that bulklike behavior is observed for water flowing through carbon nanotubes (CNTs) of diameters $\sim$1.4 nm and larger. Alternatively, the origin of the no-slip boundary condition remains an assumption that is not based on any physical principles [3]. The no-slip boundary condition is usually verified in macroscale flows while slip boundary conditions have been experimentally [4–8] and numerically [9–13] observed in nanoconfined flows. Since the pioneering work by Navier [14], a slip boundary condition was proposed as

$$u_s = L_s \left.\frac{\partial u}{\partial \xi}\right|_s, \tag{1}$$

where u_s is the slip velocity at the solid-liquid interface, L_s is the slip length, and ξ represents the coordinate normal to the solid-liquid interface. The slip length is the distance at which the linearly extrapolated velocity reaches a no-slip condition; therefore, the conventional no-slip boundary condition is the particular case for which $L_s = 0$. Equation (1) represents an empirical relation; however, it can be used to model the deviations from the no-slip boundary condition observed in nanoconfined flows.

The nature of the hydrodynamic slip phenomenon has been investigated using classical molecular dynamics (MD) simulations where the slip behavior is usually characterized by L_s. A quasiuniversal relationship between L_s and the wettability of the channels surfaces was proposed [15] for organic and inorganic surfaces, and later confirmed [16] for diamondlike surfaces having different surface roughness and wettability. In general, it is proposed that L_s is likely to be large on hydrophobic surfaces and smaller or even zero on some hydrophilic surfaces. However, Ho *et al.* [11] demonstrated that large slip can occur on hydrophilic surfaces by artificially modifying the substrate density. Voronov *et al.* [17] also found a growth of L_s as the surfaces became more hydrophilic by modifying the energy landscape roughness given by the length parameter in the solid-liquid Lennard-Jones interaction potential.

The balance between the solid-liquid binding forces, liquid-liquid cohesive forces, and flow-driving forces plays a major role in the determination of the hydrodynamic slip in nanoconfined liquids. The effect of the shear rate on the slip boundary condition in nanoconfined liquids has been a source of considerable discussion in the literature. Early investigations reported that L_s grew in an unbounded fashion as the shear rate increased [17,18], others have indicated that L_s saturates at a fixed value at high shear rates [19], and may even experience a decrease of L_s at high shear rates as has been reported in [20]. A consistent observation among several investigations is that L_s is constant at low shear rates and it is at this limit where nonequilibrium and equilibrium calculations of L_s usually coincide. Moreover, the nature of the equilibrium models of hydrodynamic slip suggests that L_s is a surface property, i.e., a parameter that does not depend on the size of the channels, but rather on the particular solid-liquid affinity. The objective of the current investigation is to evaluate the accuracy of the principal theories suggesting that L_s is a surface property using equilibrium molecular dynamics (EMD) simulations to calculate the friction factor in water confined between two graphite plates. The features of the implementation of the equilibrium theories for the calculation of L_s, such as consistency of the calculations between different independent simulations and channel-size dependence,

*Corresponding author: bra3@gatech.edu

were critically assessed. Nonequilibrium molecular dynamics (NEMD) calculations were used to verify the outcome of the equilibrium calculations using channels of different sizes. In addition, the trajectories of the liquid particles within the confinements were statistically analyzed to explain the limitations of some of the equilibrium slip theories.

II. EQUILIBRIUM THEORIES FOR THE CALCULATION OF HYDRODYNAMIC SLIP

Bocquet and Barrat [21] formulated a model for calculating L_s as an equilibrium property from a Green-Kubo-like expression. Linear response theory and the Mori-Zwanzig formalism were used independently to obtain the friction factor λ from the time-dependent correlation

$$\lambda = \frac{1}{Ak_BT}\int_0^\infty dt\langle F_x(t)F_x(0)\rangle, \tag{2}$$

where F_x is the x component of the total force acting on the solid wall due to the liquid atoms, A is the area of the wall, k_B is the Boltzmann constant, and T is the absolute temperature. Then, $L_s = \eta/\lambda$, where η is the shear viscosity. An inherent property of the dissipation coefficients calculated by Green-Kubo-like expressions in finite systems is that integrals similar to the one in Eq. (2) tend to vanish as the lag time approaches infinity. This issue was acknowledged in [21] and it was also indicated that some authors have proposed a practical solution to this problem. One approach to perform these calculations is by setting the upper limit of the autocorrelation integral as the first zero of the autocorrelation function. In so doing, Bocquet and Barrat [21] found good correlation between the EMD calculations of L_s and their own phenomenological model.

Petravic and Harrowell [22] challenged the idea that the calculation of L_s as derived from Eq. (2) was an intrinsic surface property. By performing a series of calculations of λ and L_s in nanochannels having walls made of dissimilar materials and different sizes, Petravic and Harrowell [22] observed size-dependent and material-independent values of λ. It was also indicated that during the development of the model for obtaining Eq. (2), an incorrect identification of the slip velocity was made in [21], thereby introducing an unrealistic correlation between slip and the shear force acting on the walls. Petravic and Harrowell [22] formulated an equilibrium perturbation problem based on Doll's equations of motion. A perturbation was introduced into the system by a relative velocity (Δv_{wall}) between the confining walls and the linear response of the system was analyzed in the limit of small Δv_{wall} to obtain a new friction coefficient, μ:

$$\mu_i = \lim_{\Delta v_{\text{wall}}\to 0}\frac{\langle F_{xi}(t)\rangle/A}{\Delta v_{\text{wall}}} = \frac{1}{Ak_BT}\int_0^t dt\langle F_{xi}(t)F_{xi}(0)\rangle, \tag{3}$$

where the subscript i denotes any of the confining channel walls and μ_i is evaluated as $t\to\infty$. When equilibrium is reached, $\mu_1(t) = \mu_2(t) = \mu$. Equation (3) is similar to Eq. (2) except for the fact that Δv_{wall} is used instead of the slip velocity in the relationship between friction force and velocity, during the development of the model. Therefore, Eq. (3) encompasses the entire thickness of the confined fluid, which led to the explanation of the size dependence of λ reported in [22]. The calculation of L_s was modified as follows:

$$L_s = \frac{1}{2}\left(\frac{\eta}{\mu} - H\right), \tag{4}$$

where H is the separation between the nanochannel confining walls. It is important to note that Eq. (4) only pertains to a system with similar walls.

Hansen *et al.* [23] supported the argument that Eq. (2) accounts for the friction of the entire system (interfacial plus bulk) and indicated the necessity of isolating the wall-affected region from the bulk in order to obtain the actual interfacial friction. Hansen *et al.* [23] followed Navier's original work and formulated the wall friction problem for a slender liquid slab of thickness Δ near the wall. By performing an analysis of the wall-slab, bulk-liquid-slab, and external force interactions, the following expression was obtained for correlating the slab velocity-force and velocity-velocity time correlations in the Laplace space:

$$\tilde{C}_{uF_x'}(s) = -\sum_{i=1}^{n}\frac{B_i\tilde{C}_{uu}(s)}{s+\kappa_i}, \tag{5}$$

where the autocorrelation functions in the time domain are

$$C_{uF_x'}(t) = \langle u_{\text{slab}}(0)F_x'(t)\rangle \text{ and } C_{uu}(t) = \langle u_{\text{slab}}(0)u_{\text{slab}}(t)\rangle, \tag{6}$$

and the force and slab velocity can be determined from EMD simulations as

$$F_x'(t) = \sum_{\substack{i\in\text{slab}\\ j\in\text{wall}}} F_{ij,x}(t) \text{ and } u_{\text{slab}}(t) = \frac{1}{m}\sum_{i\in\text{slab}} m_i v_{i,x}(t). \tag{7}$$

The wall-slab friction force was modeled using a Maxwellian memory function for convenience purposes. Then, the friction coefficient was obtained by fitting the parameters B_i and κ_i in Eq. (5) and the zero-frequency friction coefficient was given by $\lambda_0 = \zeta_0/A$, where $\zeta_0 = B_0/\kappa_0$ and A is area. Hansen *et al.* [23] found that ζ_0 was Δ dependent and that different trials must be conducted before finding the appropriate value of Δ. Slabs of small width did not account for the whole wall-slab interactions and thicker slabs included unwanted bulk effects. It was observed that the friction coefficient was channel-width dependent for channels with $H \leqslant 7\sigma$, where σ represents the liquid molecular diameter.

Bocquet and Barrat [24] responded to the previous criticisms of their model by implying that such observations were delicate and subtle issues caused mainly by the order in which the thermodynamic limit and the time approaching to infinity limit are taken from the EMD simulations. In order to prove the validity of the previous model, Eq. (2), a new derivation of the friction coefficient λ was developed in [24]. A more fundamental formulation based on the general Langevin equation applied to both planar and cylindrically confined fluids was developed and the previous expression for λ was verified; see Eq. (2).

Huang and Szlufarska [25] recognized a main issue in the discussion about the friction coefficients obtained from equilibrium calculations. It was indicated that λ is not a bulk property but a local parameter. For example, solid-liquid friction exists in liquids flowing through a carbon nanotube but it is impossible to obtain the thermodynamic limit in such

a system, as required and indicated by Bocquet and Barrat [21,24]. Likewise, in the presence of heterogeneous walls or liquid mixtures flowing past a solid, a bulk property expression such as Eq. (2) is not able to capture the inhomogeneity of the local interfacial region where friction occurs. Huang and Szlufarska [25] proposed to analyze the linear response of individual liquid particles at the solid-liquid interface after applying a perturbation. Difficulties were found in obtaining a well-defined size of the interfacial region, which was solved by using the generalized Langevin equation. The resulting expressions for the calculation of the friction coefficient are

$$\lambda(\omega) = \frac{1}{Ak_BT[1-\alpha(\omega)]} \sum_i \int_0^\infty dt \langle F_i(0)F_i(t)\rangle e^{j\omega t}, \quad (8)$$

and

$$\alpha(\omega) = \frac{1}{Ak_BT} \sum_i \int_0^\infty dt \langle F_i(0)u_i(t)\rangle e^{j\omega t}, \quad (9)$$

where the short-range nature of the interaction between the wall and individual liquid particles F_i allows Eqs. (8) and (9) to be evaluated using all of the liquid particles in the confinement without affecting the interfacial nature of the calculations. The static friction factor, $\lambda(0)$, can be used to obtain the slip length as $L_s = \eta/\lambda(0)$. Huang and Szlufarska [25] calculated λ for different fluids using NEMD and EMD [Eqs. (8) and (9)] having different solid-liquid affinity conditions. Good correlation was found between the NEMD and EMD simulations. Huang and Szlufarska [25] observed that the integral in Eq. (8), for $\omega = 0$, reaches an equilibrium value of λ, whereas the integral in Eq. (2) is rather noisy and area dependent. Moreover, the equilibrium calculations of λ using Eq. (8) fell within the error margins of the NEMD simulations, while the results obtained using Eq. (2) underpredicted the NEMD results.

Both supporting and contradicting arguments about the reliability of the equilibrium friction model derived by Bocquet and Barrat [21,24] can be found in the literature. Some authors have reported smooth time-dependent λ calculations using Eq. (2) with a plateau over which the steady-state value of λ was evaluated [22,26–29]. Furthermore, consistency between EMD calculations of L_s using Eq. (2) and NEMD simulations has been observed [26,28,29]. Additionally, size-independent calculations of L_s, supporting the idea that Eq. (2) predicts a surface property, can be found [26]. Alternatively, noisy and marginally reliable calculations of λ using Eq. (2) have been reported in [25,30] and also size-dependent L_s calculations in nanochannels with $H \leqslant 3$ nm [28]. New methods of analysis [23,25] and reinterpretations of the model proposed in [22] have been reported, but have not been extensively explored [31,32]. A clear controversy exists regarding the EMD calculations of solid-liquid friction and further extensive investigations are needed before drawing sound conclusions. The methods of analysis and simulation are not deeply explained in the literature and probably the differences observed throughout this literature review can be attributed to miscalculations during postprocessing or data sampling during the EMD simulations.

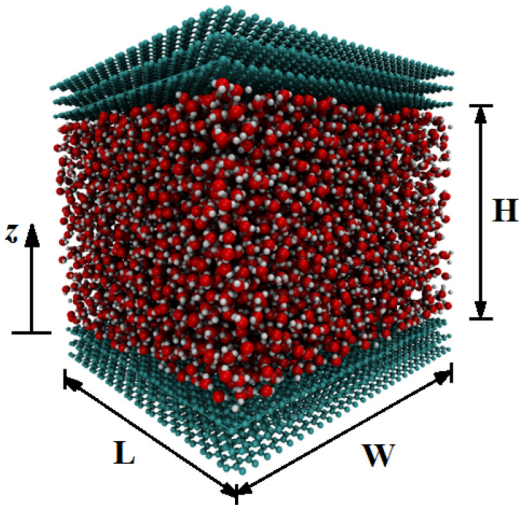

FIG. 1. Water confined between graphite plates used for the EMD and NEMD simulations of hydrodynamic slip.

III. MOLECULAR DYNAMICS MODEL AND CALCULATIONS

Equilibrium and nonequilibrium molecular dynamics simulations were conducted to investigate hydrodynamic slip for water confined between graphite plates. The SPC/E [33] water model was used due to its good predictive capabilities and for comparison purposes with previous investigations. The Coulombic interactions in the water model were treated with the PPPM algorithm [34] with an accuracy of 1×10^{-6} and the rigidity of the model was enforced through the SHAKE algorithm [35]. Graphite was modeled as a set of three graphene layers on each side of the confinement as illustrated in Fig. 1, where the outermost layers were kept fixed in order to keep a constant system size. The area of the nanochannel was constant and given by $L = 6.39$ nm and $W = 6.64$ nm, while the channel height was varied as $H = 3 - 8$ nm. The number of water molecules inside the channel was varied so that the bulk and interfacial properties remained similar for channels with different heights. The Tersoff potential [36] was used to model the atomic interactions per carbon layer and a Lennard-Jones potential with parameters $\sigma_{CC} = 3.41$ Å and $\varepsilon_{CC} = 0.298$ kJ/mol [37] was used for the interlayer carbon interactions. The water-carbon interaction potential was calibrated to obtain an experimental contact angle of 64.4° (contact angle on a clean graphitic surface [38]) from size-independent molecular dynamics simulations of graphite wettability [39]. The truncated Lennard-Jones potential parameters are $\sigma_{CO} = 3.19$ Å, $\varepsilon_{CO} = 0.4736$ kJ/mol, and $r_c = 15$ Å. The MD code LAMMPS [40] was used to perform the simulations and the software VMD [41] for visualizations purposes. All of the simulations underwent the same initial equilibration process: (1) energy minimization for eliminating any excess potential energy from the initial configuration; (2) equilibration of the system in contact with a thermal bath at 300 K using the Nosé-Hoover thermostat [42,43] with a time constant of 0.1 ps during a total time of 1 ns; (3) microcanonical ensemble run for 1 ns. All of the simulations were carried out using a time step of 1 fs.

The theories discussed in Sec. II were implemented for the equilibrium calculation of the hydrodynamic slip length. After equilibration, the coordinates and velocities for the individual atoms were recorded every 10 fs for a total production run of 1 ns. Subsequently, the atom coordinates file was used to rerun a simulation where only oxygen-carbon interactions were considered in order to isolate the solid-liquid interactions for every single particle. The x component of the force acting on each solid and liquid particle was recorded and postprocessed according to the requirements of each particular theory. For the Bocquet and Barrat model [21,24], F_x in Eq. (2) was calculated as the sum of the forces acting on each solid atom, for each wall. The same procedure was followed for the calculations required by Petravic and Harrowell [22]. Equation (7) was used to calculate the force and velocity of an interfacial slab as required by Hansen *et al.* [23]. The thickness of the slab was varied as suggested in [23]. Finally, the information gathered after isolating the solid-liquid interactions was directly incorporated into Eqs. (8) and (9) for the theory developed by Huang and Szlufarska [25]. As for the necessary discrete time-correlation calculation, the unbiased and biased algorithms [44], Eqs. (10) and (11), respectively, were used for comparison purposes,

$$\langle B(t)B(0)\rangle_k = \frac{1}{M-k}\sum_{n=0}^{M-k-1} B(t_{n+k})B(t_n) \quad \text{where } k = \{0,1,2,\ldots,M-1\}, \tag{10}$$

$$\langle B(t)B(0)\rangle_k = \frac{1}{M}\sum_{n=0}^{M-k-1} B(t_{n+k})B(t_n) \quad \text{where } k = \{0,1,2,\ldots,M-1\}. \tag{11}$$

where B is a time-dependent function, such as F_x, F_i, or u_i; k is the discrete lag-time index; and M is the total number of elements in the lag-time sample of B.

Couette and Poiseuille flow simulations were conducted using NEMD to determine L_s from the resulting velocity profile, such that

$$L_s = \frac{\Delta u_s}{\partial u/\partial z|_{z_0}}, \tag{12}$$

where Δu_s is the relative velocity between the liquid and the solid wall at the interface and $\partial u/\partial z|_{z_0}$ is the velocity gradient evaluated at the position $z_0 = 0$. Couette flow was generated by moving the upper wall of the channel depicted in Fig. 1 at a constant velocity in order to create a shear flow. The shear rate experienced by the system was changed by varying the velocity of the moving wall in channels of different size ($H = 3-8$ nm). Poiseuille flow was generated by applying a body force to each liquid particle in the x direction. The magnitude of the force was varied in channels with different sizes while the shear rate was recorded. The velocity, pressure, and density profiles were obtained by means of time averaging of the particle count and velocity and pressure as measured in discrete bins in the z direction. The nonequilibrium simulations were run for 5 ns after equilibration, and then for an extra production run of 2 ns where the atomic velocities and coordinates were recorded every 0.5 ps. Only the carbon atoms were thermostated during the NEMD simulations to ensure natural cooling through the walls.

IV. RESULTS AND DISCUSSION

A. Nanoconfined water with similar bulk and interfacial properties

The number of water molecules per unit volume was adjusted in order to eliminate any confinement effects on the interfacial and bulk properties of water in nanochannels of different sizes. Equilibrium simulations were conducted in the canonical ensemble as indicated in Sec. III for 1 ns; afterwards, the water particle coordinates were recorded every 0.5 ps during a total time of 0.5 ns; additionally, the shear stress per water molecule was recorded every 0.5 ps for a total production run of 3 ns. The water density profiles were calculated by dividing the height, H, of the nanochannels, see Fig. 1, into bins where the number of water molecules was counted and averaged over time. The size of the bins was small enough to capture the fine interfacial details and large enough to avoid losing statistical significance. Figure 2(a) depicts the water density distribution along the height of nanochannels of different sizes. Clearly, the bulk density of water is similar for every system, $\sim$1 g/cm^3. More importantly, the interfacial water structure is similar for the different nanochannels. The equilibrium calculations of L_s are based on short-range interactions between the solid walls and the

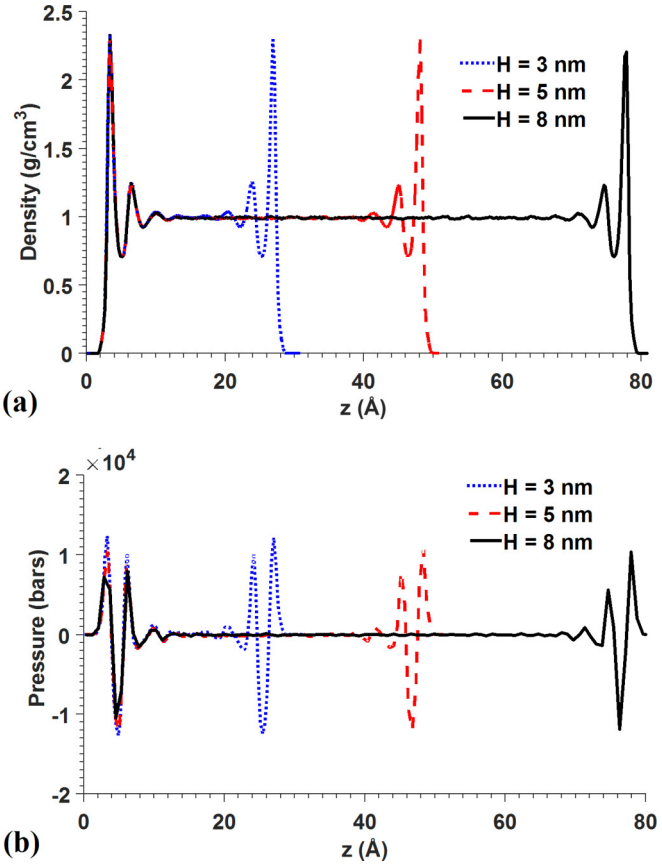

FIG. 2. Bulk and interfacial (a) density and (b) pressure profiles in nanochannels of different sizes.

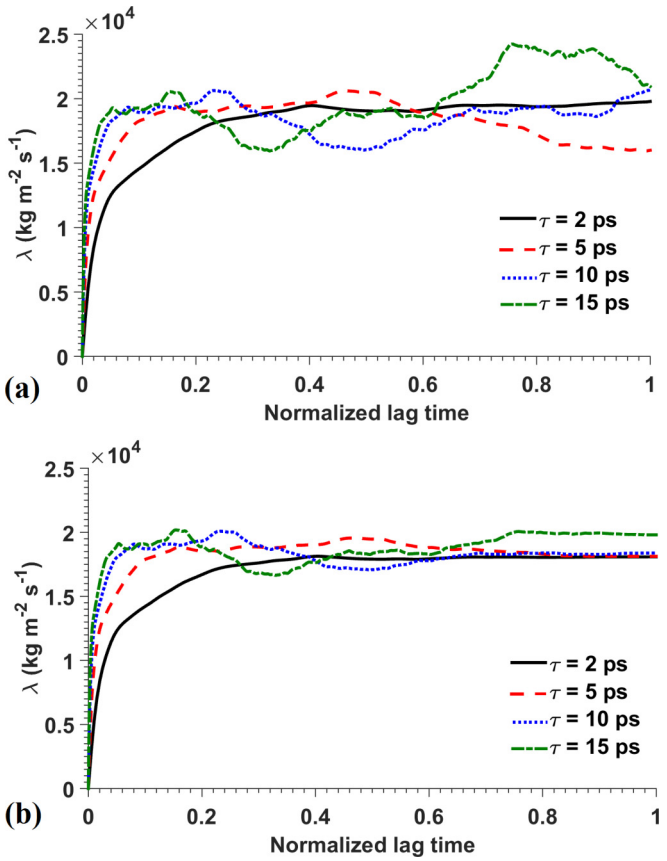

FIG. 3. Calculation of the friction coefficient, λ, using Eq. (2) with (a) unbiased and (b) biased algorithms for the evaluation of the time-correlation function.

water molecules—hence, the importance of the interfacial concentration of liquid particles.

Figure 2(b) illustrates the pressure profiles along the height of nanochannels of different sizes. The observable bulk pressure is on average ∼0 bars, but a closer look at the pressure curves reveals a variation between −200 and +200 bars. Unlike the density profiles, the interfacial pressure features small differences for the different channels; however, this can be explained due to the well-known noisiness associated with MD calculations of pressure, especially at solid-liquid interfaces where water particles concentrate.

B. Main features of the calculations of the friction coefficient using different theories

After ensuring that similar bulk and interfacial liquid water structures existed in the different nanochannels, the characteristics of the calculations of the friction coefficient, λ, were investigated using different theories. Initially, the effect of the lag time, τ, used in the evaluation of the time-correlation function (TCF) formulated by Bocquet and Barrat [21,24], was analyzed. Data were recorded for a total time of 1 ns using a nanochannel height of $H = 5$ nm. Different lag times were used to evaluate Eq. (2) with a time interval of 0.1 ps between TCFs. Figure 3(a) depicts the calculation of λ using an unbiased algorithm [Eq. (10)] for the evaluation of the TCF, and the values of λ are depicted as running integrals, with the lag time normalized, so as to observe if saturation occurs. The evaluation of λ using Eq. (2) appears to be reliable only for the shortest lag time, $\tau = 2$ ps, just as indicated in [21] and observed in [26,27], where the value of λ can be obtained from the observed plateau. As the lag time for the evaluation of the TCF increases, the noise associated with the calculations increases accordingly such that there is no observable plateau. Huang and Szlufarska [25] observed a similar behavior when employing Eq. (2).

If the TCF of Eq. (2) is evaluated with a biased algorithm, see Eq. (11), the previous calculation of the friction coefficient is significantly modified as illustrated in Fig. 3(b). The noisiness of the integral of Eq. (2) decreases and λ seems to saturate at a value similar to that for $\tau = 2$, 5, and 10 ps. The difference in the calculated values using the biased and unbiased algorithms is due to the normalization performed on the discrete calculation of the lag-time shift in the time-correlated functions. The unbiased algorithm weighs the sum of the products as $M - k$, which is consistent with the number of operations performed (k approaches M). Alternatively, the biased algorithm always normalizes the number of products by M. If the analyzed function B, see Eqs. (10) and (11), loses correlation as the lag time increases, it is expected that the last terms in the series of Eq. (10) account only for weakly correlated products and the weight of the normalization given by $M - k$ would not dampen the expected noise. Thus, the biased algorithm features a smaller standard deviation for the calculation of the TCFs and it is usually preferred by the signals and systems community [44].

Smooth running integrals of λ using long dimensionless lag times were observed in [22] and using a lag time of 12 ps in [29]. It has been demonstrated that using biased algorithms for the evaluation of the TCF in Eq. (2) leads to smoother time-dependent λ curves, which could be one of the reasons why some authors report noisy and others smooth λ curves. In most publications, little or no information is given about the specific details of the postprocessing stage, but as has been shown here, drastically different results can be obtained by simply modifying the algorithm used for data postprocessing.

The characteristics of the calculation of $\lambda = \lambda(0)$ by implementing Eqs. (8) and (9) are depicted in Fig. 4. It was

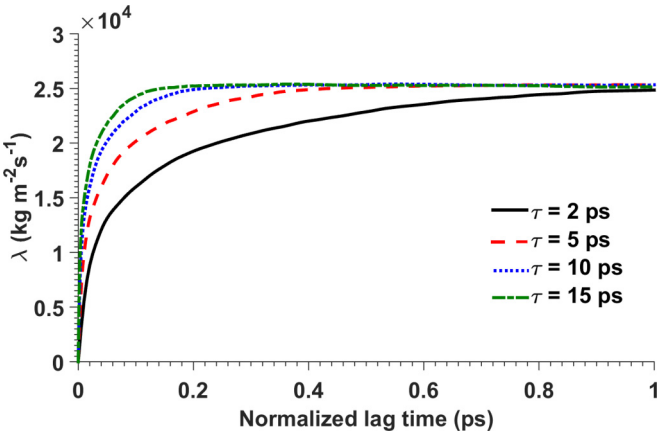

FIG. 4. Calculation of the friction coefficient λ using Eq. (8) as suggested by Huang and Szlufarska [25].

verified that the value of α, obtained from Eq. (9), has a negligible impact on λ as indicated by Huang and Szlufarska [25]. Equilibrium values of $\alpha(0) \sim 10^{-6}$ were obtained, and thus neglected at the cost of no distinguishable impact on λ but gaining efficiency during the postprocessing stage and savings in storage. The effect of using different lag times for the evaluation of the TCF in Eq. (8) is depicted in Fig 4. Smooth running integrals of λ are observed for different lag times; additionally, all of the curves saturate at the same plateau, making possible a reliable calculation of λ in equilibrium. From this, it can be inferred that one of the reasons for which the model developed in [25] leads to smoother calculations than Eq. (2), is that the sum of several individual TCFs of the solid-liquid interaction forces are considered in the calculation of λ, in addition to the fact that Eq. (2) is based on the lumped sum of forces for a given number of solid particles. For statistical purposes, Eq. (8) presents a better alternative than Eq. (2) and also offers the possibility of applications involving heterogeneous systems, since the analysis is performed on the liquid particles. It is also important to note that a negligible effect is observed from using the biased or unbiased algorithms for the evaluation of the TCFs.

Finally, the method used in the calculation of λ reported by Hansen *et al.* [23] was evaluated. Equations (7) were used to calculate the properties of the interfacial liquid slabs with dimensions varying between 1 and 3 water molecular diameters. The biased algorithm was used to evaluate the TCFs depicted in Eqs. (6) for different lag times. It was observed that while the velocity autocorrelation function $\langle u_{\text{slab}}(t)u_{\text{slab}}(0)\rangle$ always featured a relatively smooth behavior, the force-velocity cross correlation $\langle F_x{}'(t)u_{\text{slab}}(0)\rangle$ was considerably noisier. The best illustration of this is depicted in Fig. 5(a) for a rather short lag time of 1 ps. The Laplace transform of the TCFs shown in Fig. 5(a) is depicted in Fig. 5(b). As illustrated, the noisiness of $\langle F_x{}'(t)u_{\text{slab}}(0)\rangle$ is reduced in the Laplace space; however, the fitting process suggested in Eq. (5) is conducted to obtain slab-size and lag-time-dependent values of λ. In personal communications with the authors of [23] and [32] (where the method reported in [23] was applied to water-graphene systems), it was disclosed that the implementation of this method is quite problematic for water and usually requires a large number of simulations to achieve a reliable value of λ. Therefore, due to its high complexity, high computational demand, and sensitivity of L_s to the definition of the interfacial region, the equilibrium model reported by Hansen *et al.* [23] was not utilized to calculate the value of L_s in this investigation.

C. Calculation of the hydrodynamic slip length in nanochannels of different sizes

Data were collected from six independent simulations for each nanochannel size, $H = 3$, 5, and 8 nm. The time-dependent total force was recorded for the top and bottom walls for the calculations involving Eqs. (2) and (4), while the forces acting on each liquid particle, its coordinates, and velocities were recorded for utilization in Eq. (8). According to Bocquet and Barrat [21,24], the hydrodynamic slip length is given by $L_s = \eta/\lambda$, where $\eta = 0.792 \times 10^{-3}$ Pa s is the shear viscosity of SPC/E water [45] and λ is obtained from

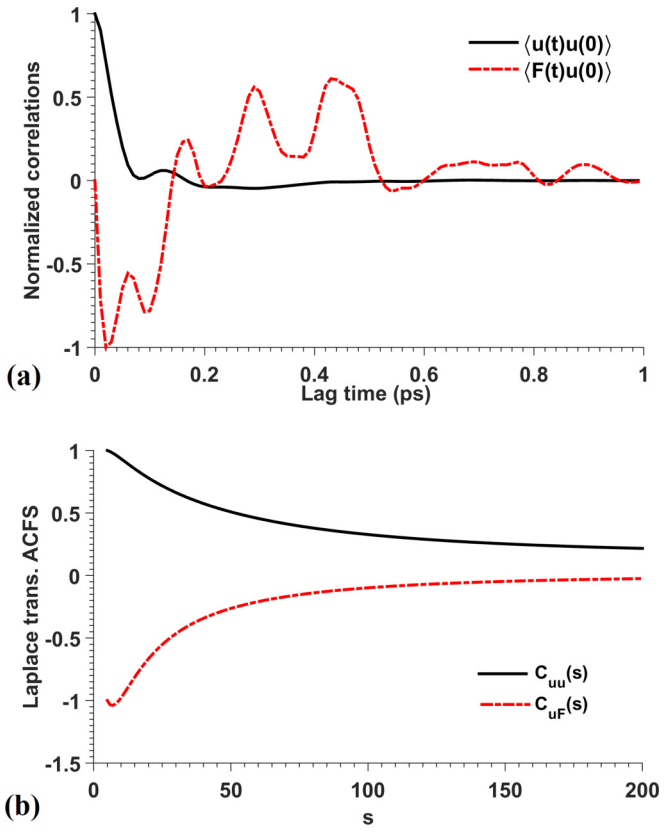

FIG. 5. Implementation of the method of Hansen [23] for calculating the liquid slab normalized (a) time-correlation function and (b) the Laplace-transformed correlation functions.

Eq. (2). Twelve different lag-time-dependent curves of λ were averaged (six independent runs times two confining walls) for each nanochannel and then L_s was recorded in Fig. 6. Two aspects can be highlighted from this first set of simulations: (1) the steady-state value at the plateau of the λ curves notably varied between independent simulations as it can be observed in Fig. 6 for the Bocquet and Barrat [21,24] group of curves. The error bars at the end of each curve represent the standard deviation of the value of L_s and each curve is the average of 12

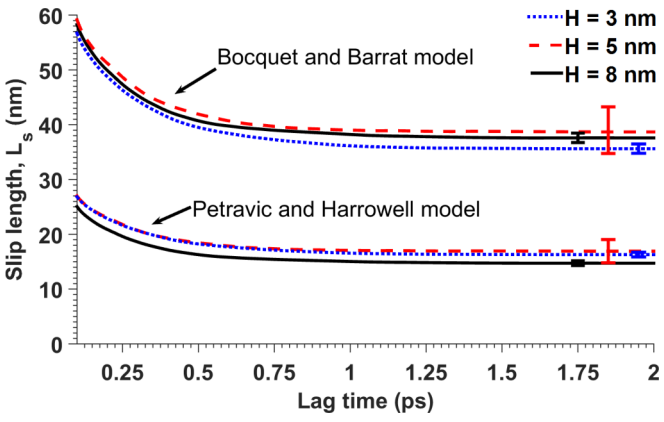

FIG. 6. Calculation of the hydrodynamic slip length using Eq. (2) and $L_s = \eta/\lambda$, Bocquet and Barrat model [21,24] (upper curves); and using Eqs. (3) and (4), Petravic and Harrowell model [22] (lower curves).

different curves. (2) It was continuously observed that the L_s curve for $H = 3$ nm was always the lowest, indicating a trend towards a smaller value of L_s for a highly confined channel. As for the identification of L_s as a surface property, the large margin of error in the calculations using Bocquet and Barrat [21,24] theory makes this assessment difficult. It is possible to identify a large region where L_s could be defined as a surface property; however, the consistent observation of L_s being the lowest for the nanochannel with $H = 3$ nm calls for further analysis.

The reinterpretation suggested by Petravic and Harrowell [22] to the theory proposed in [21,24] was implemented by applying Eqs. (3) and (4). Evidently, Eq. (3) is the same as Eq. (2) as $t \to \infty$, but this implementation is not possible, due to the increased noisiness of the TCFs as $t \to \infty$; therefore, the λ curves previously obtained were used for the calculation of L_s as indicated in Eq. (4). Six independent simulations were averaged and the resulting L_s curves are depicted in Fig. 6 where the error bars indicate the standard deviation of L_s at the plateau. Since these new calculations of L_s depend upon the λ values previously obtained, the large error bars previously observed for $H = 5$ nm are still present. Two aspects can be highlighted about the implementation of Petravic and Harrowell [22] theory: (1) the values of L_s for the different nanochannels decreased by approximately a factor of 2 compared with the predictions using Eq. (2) and $L_s = \eta/\lambda$; this was also observed in [22]. (2) The implementation of Eq. (4) seems to verify L_s as a surface property for the two smallest nanochannels; however, the large error bars observed for $H = 5$ nm again hinder any definite claim about the nature of L_s. On a final remark, it must be remembered that although the calculation of the friction coefficient using the models by Bocquet and Barrat [21,24] and Petravic and Harrowell [22] are similar, they significantly differ in how L_s is calculated. Both models are radically different based on the interpretation of the correlation between the friction coefficient and the perturbation used to induce flow; see Sec. II.

Huang and Szlufarska [25] indicated that due to the short-range nature of the interaction between the solid walls and the liquid particles, Eq. (8) can be applied to an interfacial region near the solid walls or to the whole liquid domain; however, the authors of [25] did not indicate that in order to apply Eq. (8) to the total number of liquid particles confined within the walls of a nanochannel, a normalization by $2A$ is necessary. This was confirmed by means of evaluating Eq. (8) in particles confined within interfacial regions near a solid wall. The extent of the interfacial space was increased until reaching half of the domain, where λ matched the value obtained from evaluating the total number of liquid particles using Eq. (8) normalized by $2A$. In order to avoid errors associated with the correct definition of the interface, all of the liquid particles within the confinement were included in the calculation of λ and the corresponding lag-time-dependent calculations of L_s are illustrated in Fig. 7. A remarkable difference between the consistency of the calculations of L_s using Huang and Szlufarska's [25] theory can be observed when compared with the previous two analyzed theories. The L_s curves depicted in Fig. 7 are the result of averaging six independent simulations for each nanochannel size and as it can be observed the magnitude of the larger error bars is $\sim$1 nm. More importantly,

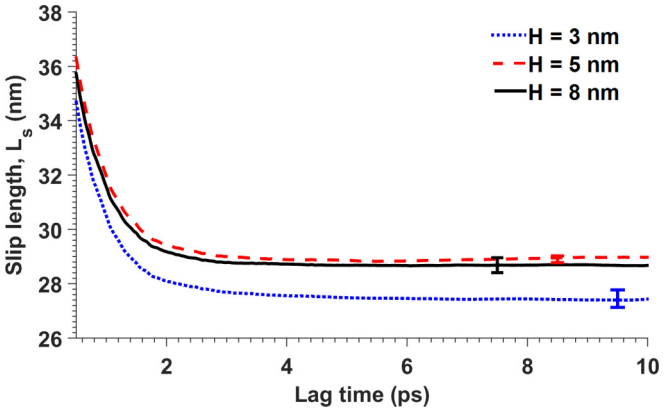

FIG. 7. Calculation of the hydrodynamic slip length using Eq. (8) and $L_s = \eta/\lambda$ [25].

the consistency of these calculations allows observing that the theory by Huang and Szlufarska [25] predicts that L_s is size independent when the channel size is $H \geqslant 5$ nm. In addition, the accuracy of these calculations allows to verify that the smallest nanochannel features the smallest value of L_s, eliminating any uncertainty due to the variation observed between different simulations as in the calculations using Bocquet and Barrat [21,24] theory. Another aspect to highlight is that the prediction of L_s by Huang and Szlufarska [25] lies between the previously analyzed theories.

Irrespective of the different formulations leading to the theories reported in [21,24,25], and disregarding the fact that the predictions of L_s differ in magnitude using these two models, both indicate that L_s for the nanochannel with $H = 3$ nm is smaller than that for the larger channels considered. Further analysis was conducted in an effort to clarify the reason for this observation. For a model to predict L_s as a surface property, it must quantify the short-range nature of the solid-liquid force interactions at the interface, just as in Eqs. (2) and (8). These interactions originate from a number of interfacial liquid particles—thus the reason for the verification of the interfacial liquid structure at the beginning of Sec. IV. However, not only a time-averaged fixed concentration of interfacial liquid particles must be observed, but also the presence of the "same" particles, namely, mobility is important as well. If the range of mobility of liquid particles within a nanochannel is such that some particle can move from the bulk to the interfaces, the contribution to the forces reported on these liquid particles and the corresponding effect on the solid atoms due to proximity, observed in Eqs. (2) and (8), are reflected in the force TCFs and hence in the L_s calculation from λ.

The trajectory of individual water molecules was tracked over the entire simulation time in the different nanochannels. The time average and standard deviation of the trajectory of each molecule was analyzed in order to observe the mobility of the particles. The upper panels of Fig. 8 represent the information obtained for the smallest nanochannel. The scatter plot indicates that many of the bulk particles have a large mobility within the 3-nm nanochannel and the histogram of the mean position indicates that a large number of water molecules tend to remain in the bulk. The density profiles depicted in Fig. 2(a) demonstrate that when averaged over

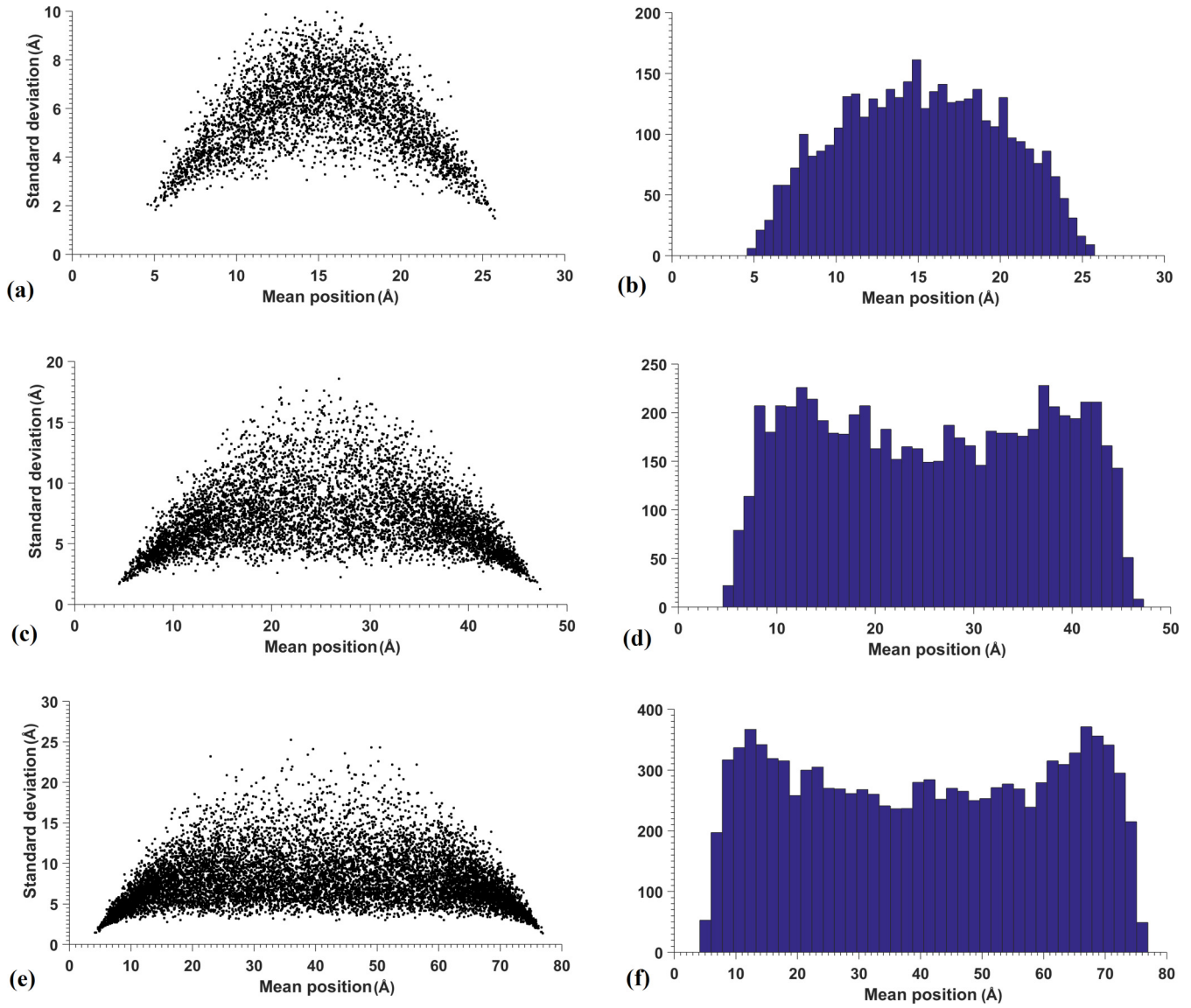

FIG. 8. Statistical analysis of the displacement of the liquid molecules confined in nanochannels: $H = 3$ nm, upper panels (a,b); $H = 5$ nm, middle panels (c,d); and $H = 8$ nm (e,f). The right panels are histograms of the time-average position of the liquid particles and the left panels are plots of the average versus standard deviation position of the liquid particles in the confinement.

time in fixed regions, the interfacial concentration of liquid particles is the same for each nanochannel, the histogram of the average position of the particles indicates that most of them tend to remain at the center of the channel, and the scatter plot illustrates that the bulk particles have a large mobility. Hence, a number of particles can travel from the bulk to the interface and back contributing to the force TCFs observed in Eqs. (2) and (8) increasing the value of λ and hence reducing the expected L_s. Alternatively, the middle and bottom panels of Fig. 8 clearly depict two population peaks of liquid particles near the solid walls in the histograms of the average position of individual particles. Likewise, the scatter plots illustrate a large concentration of particles near the walls where the mobility of liquid particles is limited by the strong solid-liquid interaction. Contrary to what was observed in the 3-nm channel, the number of bulk liquid particles with the sufficient mobility to travel from the bulk to the interfaces is dramatically reduced in the 5- and 8-nm channels, thus explaining the consistency between the L_s calculations observed in Fig. 7.

D. Nonequilibrium calculations of the slip length

Poiseuille and Couette flows were simulated in nanochannels of different sizes with $H = 3$, 5, and 8 nm. Shear flow was induced by moving the upper wall at a constant velocity while the bottom wall remained unaltered. Poiseuille flow was generated by means of exerting a variety of force magnitudes on the liquid particles ranging from 1×10^{-7} to 1×10^{-6} eV/Å. Since different channel sizes and flow types were used to obtain L_s from NEMD simulations, and in order to verify the low shear rate limit consistency with EMD simulations, L_s was recorded as a function of the shear rate. Figure 9 depicts the results obtained from the NEMD simulations, where the symbols represent the average

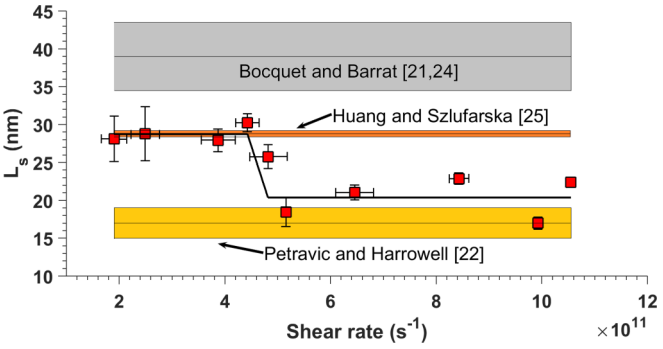

FIG. 9. Comparison between nonequilibrium (solid symbols) and equilibrium (shaded regions) calculations of L_s.

of a number of independent simulations, in terms of L_s and shear rate, and the error bars are the range of variation observed for each set of simulations. The symbols represent the average between independent simulations for channels of all sizes, although it must be indicated that for shear rates $\leqslant 4 \times 10^{11}\ s^{-1}$, the results for $H = 3$ nm were very noisy. The following can be summarized from these modeling efforts: (a) consistent with the trends reported in [20] for nanoconfined flows with a deficient thermal energy removal through the channels walls, L_s decreased as the shear rate increased; this is due to the increased number of liquid particle collisions with the solid walls due to overheating; (b) size effects were difficult to observe due to the noisiness generated in the NEMD calculations of L_s using Eq. (12) for the smallest nanochannel, although the simulation results for the larger channels were very consistent; and (c) it can be observed that Huang and Szlufarska's theory was the best fit to the NEMD calculations of L_s in the low shear rate limit. Hence, this equilibrium approach is highly encouraged as an alternative to time-consuming NEMD simulations.

V. CONCLUSIONS

A number of theories suggesting that the hydrodynamic slip length is an intrinsic surface property were critically evaluated. According to these theories, the size of the confinement would not have an effect on the observable value of L_s, as suggested from some of the Green-Kubo-like expressions found in these theories. The slip model reported by Hansen *et al.* [23] was disregarded since the beginning of this investigation due to the low reliability and consistency of the calculations performed to obtain L_s. Alternatively, the theories by Bocquet and Barrat [21,24], Petravic and Harrowell [22], and Huang and Szlufarska [25] posed significant advantages like shorter postprocessing times and more consistent results. The calculations of L_s using the theories reported by Bocquet and Barrat [21,24] and Petravic and Harrowell [22] were drastically hindered by the noisiness involved in the evaluation of the force time-correlation functions. The theory by Huang and Szlufarska [25] provided smoother and more consistent calculations that were not affected by the margin of error between independent simulations. This theory clearly showed size-independent L_s values for 5-nm channels and larger. The high mobility of liquid particles confined in channels as small as 3 nm was found to be the cause for observing smaller values of L_s in highly confined liquids. Nonequilibrium calculations of L_s were consistent with Huang and Szlufarska's equilibrium model, but no reliable data were extracted from the simulation for the 3-nm channel to verify the surface property nature of L_s, except for 5-nm channels and above.

ACKNOWLEDGMENTS

While performing this investigation, Bladimir Ramos-Alvarado was partially supported by the Mexican Council on Science and Technology (CONACyT) under the scholarship Grant No. 312756.

[1] L. Bocquet and E. Charlaix, Chem. Soc. Rev. **39**, 1073 (2010).
[2] J. A. Thomas and A. J. H. McGaughey, Phys. Rev. Lett. **102**, 184502 (2009).
[3] D. C. Tretheway and C. D. Meinhart, Phys. Fluids **14**, L9 (2002).
[4] D. Lasne, A. Maali, Y. Amarouchene, L. Cognet, B. Lounis, and H. Kellay, Phys. Rev. Lett. **100**, 214502 (2008).
[5] A. Maali, T. Cohen-Bouhacina, and H. Kellay, Appl. Phys. Lett. **92**, 053101 (2008).
[6] O. I. Vinogradova, K. Koynov, A. Best, and F. Feuillebois, Phys. Rev. Lett. **102**, 118302 (2009).
[7] D. Schaeffel, S. Yordanov, M. Schmelzeisen, T. Yamamoto, M. Kappl, R. Schmitz, B. Dünweg, H.-J. Butt, and K. Koynov, Phys. Rev. E **87**, 051001(R) (2013).
[8] L. Li, J. Mo, and Z. Li, Phys. Rev. E **90**, 033003 (2014).
[9] C. Liu and Z. Li, Phys. Rev. E **80**, 036302 (2009).
[10] H. Zhang, Z. Zhang, Y. Zheng, and H. Ye, Phys. Rev. E **81**, 066303 (2010).
[11] T. A. Ho, D. V. Papavassiliou, L. L. Lee, and A. Striolo, Proc. Natl. Acad. Sci. U. S. A. **108**, 16170 (2011).
[12] C. Liu and Z. Li, AIP Adv. **1**, 032108 (2011).
[13] H. Zhang, Z. Zhang, and H. Ye, Microfluid. Nanofluid. **12**, 107 (2011).
[14] C. L. Navier, Mem. Acad. Sci. Inst. Fr. **6**, 389 (1823).
[15] D. M. Huang, C. Sendner, D. Horinek, R. R. Netz, and L. Bocquet, Phys. Rev. Lett. **101**, 226101 (2008).
[16] C. Sendner, D. Horinek, L. Bocquet, and R. R. Netz, Langmuir **25**, 10768 (2009).
[17] R. S. Voronov, D. V. Papavassiliou, and L. L. Lee, J. Chem. Phys. **124**, 204701 (2006).
[18] P. A. Thompson and S. M. Troian, Nature **389**, 360 (1997).
[19] A. Martini, H. Y. Hsu, N. A. Patankar, and S. Lichter, Phys. Rev. Lett. **100**, 206001 (2008).
[20] A. Alizadeh Pahlavan and J. B. Freund, Phys. Rev. E **83**, 021602 (2011).
[21] L. Bocquet and J.-L. Barrat, Phys. Rev. E **49**, 3079 (1994).
[22] J. Petravic and P. Harrowell, J. Chem. Phys. **127**, 174706 (2007).
[23] J. S. Hansen, B. D. Todd, and P. J. Daivis, Phys. Rev. E **84**, 016313 (2011).
[24] L. Bocquet and J. L. Barrat, J. Chem. Phys. **139**, 044704 (2013).
[25] K. Huang and I. Szlufarska, Phys. Rev. E **89**, 032119 (2014).

[26] K. Falk, F. Sedlmeier, L. Joly, R. R. Netz, and L. Bocquet, Nano Lett. **10**, 4067 (2010).
[27] G. Tocci, L. Joly, and A. Michaelides, Nano Lett. **14**, 6872 (2014).
[28] N. Wei, X. Peng, and Z. Xu, Phys. Rev. E **89**, 012113 (2014).
[29] Z. Liang and P. Keblinski, J. Chem. Phys. **142**, 134701 (2015).
[30] P. Español and I. Zúñiga, J. Chem. Phys. **98**, 574 (1993).
[31] S. K. Kannam, B. D. Todd, J. S. Hansen, and P. J. Daivis, J. Chem. Phys. **135**, 144701 (2011).
[32] S. K. Kannam, B. D. Todd, J. S. Hansen, and P. J. Daivis, J. Chem. Phys. **136**, 024705 (2012).
[33] H. J. C. Berendsen, J. R. Grigera, and T. P. Straatsma, J. Phys. Chem. **91**, 6269 (1987).
[34] R. W. Hockney and J. W. Eastwood, *Computer Simulation Using Particles* (CRC Press, Boca Raton, FL, 1988).
[35] J.-P. Ryckaert, G. Ciccotti, and H. J. C. Berendsen, J. Comput. Phys. **23**, 327 (1977).
[36] L. Lindsay and D. A. Broido, Phys. Rev. B **81**, 205441 (2010).
[37] M. Shen, P. K. Schelling, and P. Keblinski, Phys. Rev. B **88**, 045444 (2013).
[38] Z. T. Li, Y. Wang, A. Kozbial, G. Shenoy, F. Zhou, R. McGinley, P. Ireland, B. Morganstein, A. Kunkel, S. P. Surwade, L. Li, and H. Liu, Nat. Mater. **12**, 925 (2013).
[39] B. Ramos-Alvarado, S. Kumar, and G. P. Peterson, J. Chem. Phys. **143**, 044703 (2015).
[40] S. Plimpton, J. Comput. Phys. **117**, 1 (1995).
[41] W. Humphrey, A. Dalke, and K. Schulten, J. Mol. Graphics Modell. **14**, 33 (1996).
[42] S. Nose, Mol. Phys. **52**, 255 (1984).
[43] W. G. Hoover, Phys. Rev. A **31**, 1695 (1985).
[44] A. D. Poularikas, *Signals and Systems Primer with* MATLAB, 1st ed., Electrical Engineering & Applied Signal Processing Series (CRC Press, Boca Raton, FL, 2006).
[45] M. A. Gonzalez and J. L. F. Abascal, J. Chem. Phys. **132**, 096101 (2010).